Int. J. Nano Dimens., 9 (2): 179-190, Spring 2018

ORIGINAL ARTICLE

Structural, magnetic and electrical properties of pure and Dy-doped Fe_2O_3 nanostructures synthesized using chemical thermal decomposition technique

Mahbobeh Jafari; Mehdi Salehi; Mahdi Behzad*

Department of Chemistry, Semnan University, Semnan, Iran

Received 27 August 2017; revised 05 December 2017; accepted 09 January 2018; available online 03 February 2018

Abstract

Pure (S_1) and Dy^{3+}-doped α-Fe_2O_3 (S_2 and S_3) nanoparticles were prepared by a combustion synthesis method at 700 °C for 8 h using $Fe(acac)_3$ (Tris(acetylacetonato)Iron(III)) as raw material. Characterizations of the prepared powders were carried out by powder X-ray diffraction (PXRD). Structural analysis was performed by the *FullProf* program employing profile matching with constant scale factors. Scanning electron microscopy (SEM), transmission electron microscopy (TEM), electrochemical impedance spectroscopy (EIS), elemental maps analysis and energy-dispersive X-ray spectroscopy (EDS) were also performed to determine the dopant amount in the α-Fe_2O_3 crystal structure (S_3). The results showed that the patterns had a main hexagonal structure with space group *R*. The cell parameters data, calculated by rietveld analysis, showed that the cell parameters were decreased with increasing the dopant (Dy^{3+}) amount in the α-Fe_2O_3 crystal structure. The average particles sizes estimated from TEM images for S_3 were about 60 nm. Besides, the magnetic properties of S_1 and S_3 were measured by vibrating sample magnetometer (VSM). It was found that with the addition of Dy^{3+} ions into the Fe_2O_3 system, the coercivity was decreased and the remanent magnetization was abruptly increased. The influence of dysprosium addition was also studied using electrochemical impedance spectroscopy. This study showed that in the presence of dysprosium ion, the charge transfer resistant increased in the electrochemical process.

Keywords: *Combustion synthesis; Electrochemical impedance spectroscopy; Magnetic property; Nano-structure characterization; X-ray powder diffraction.*

How to cite this article

Jafari M, Salehi M, Behzad M. Structural, magnetic and electrical properties of pure and Dy-doped Fe_2O_3 nanostructures synthesized using chemical thermal decomposition technique. Int. J. Nano Dimens., 2018; 9 (2): 179-190.

INTRODUCTION

Iron oxides are semiconductor materials mainly in forms of hematite (α-Fe_2O_3), maghemite (γ-Fe_2O_3), and magnetite (Fe_2O_3) [1]. Hematite (α-Fe_2O_3) with n-type semiconducting property is the most stable form of iron oxide found in nature. α-Fe_2O_3 exhibits high resistance to corrosion; therefore, it has been extensively used in many fields which include photo-anode for photo assisted electrolysis of water. It is an active component of catalysis, pigments, sorbents, magnetism, gas sensors, clinical therapy, lithium ion battery and oxidizer in thermite composition. It is also used in magnetic fluids, also called ferrofluids, for damping in inertial motors, shock absorbers, heat transfer fluids, etc. [2–7]. Different allotropes of iron oxide show semiconducting properties [1]. Hematite (α-Fe_2O_3) is an n-type semiconductor and is the most stable form of iron oxide found in nature. Fe_2O_3 nanomaterials have received great attention due to their remarkable properties in experimental fields such as catalysis, pigments, sorbents, magnetism, gas sensors, clinical therapy and etc. [2–7]. Their properties can be controlled by changing the crystallite size, synthesis techniques, surface to volume ratio, and also by changing the growth temperature [8, 9]. Synthesis of Fe_2O_3 nanomaterials from

* Corresponding Author Email: msalehi@semnan.ac.ir

Fe containing complexes, have been previously reported. However, the type of the complex has a main factor on the properties of the obtained materials.

The use of metal complexes as precursors may be useful to manipulate the purity and morphology of the obtained nanomaterials [10]. Several methods have been reported for the synthesis of Fe_2O_3 nanomaterials, including solvothermal method, sol-gel synthesis, chemical vapor deposition and etc. [11-16]. Combustion synthesis has been reported as a new, simple, inexpensive and rapid method, which allows effective production in industrial scales [17, 18]. Several metal ions have been previously doped into the α-Fe_2O_3 lattice including Al [19], Mo [20], Cr [20], Ti [21], Si [21, 22], Zn [23] and Nd [24]. Dysprosium (III) oxide (Dy_2O_3) is another potential candidate.

It is a highly insoluble and thermally stable material with high resistivity, large energy band, and high dielectric constant. Dy_2O_3, as well as numerous other functional materials based on dysprosium oxides, have been developed for a variety of applications. For instance, Dy_2O_3 is used as a photoluminescent and thermoluminescent material [25]. Dy_2O_3-based memory devices have shown excellent resistive switching behaviors. It has also shown the potential for application in magnetic resonance imaging (MRI) contrast agents in high magnetic fields owing to its excellent relaxation and relaxometric properties [26]. Because of the above mentioned descriptions, we decided to use Dy^{3+} as a dopant into Fe_2O_3 crystal system. Besides, there is no report on the synthesis of Dy^{3+} doped Fe_2O_3, and the influence of f-block elements on its crystals properties have been ignored.

In this study, $Fe(acac)_3$ was used as the precursor to produce nanostructured α-Fe_2O_3 by a simple combustion synthesis method (Fig. 1.). To the best of our knowledge, there is no report on the synthesis of the target by these reaction conditions. Furthermore, doping of Dy^{3+} into the Fe_2O_3 crystal structure is reported for the first time by the substitution route. The effect of the lanthanide dopant on the physical properties such as particle size and morphology, crystallite size, and optical properties is reported for the first time. The effect of different concentrations of Dy^{3+} doping was investigated on the magnetic property of the pure and doped α-Fe_2O_3 materials.

EXPERIMENTAL

Materials and physical measurements

Analytical grade chemicals and solvents were purchased from commercial sources and used without further purification. FT-IR spectra were obtained as KBr plates on a FT-IR SHIMADZU spectrophotometer in the 400–4000 cm^{-1} range. PXRD patterns were recorded on a Bruker AXS diffractometer D8 ADVANCE with Cu-Kα radiation with nickel beta filter in the 2θ range of 30-80°. The TEM images were obtained from a JEOL JEM 1400 transmission electron microscope with an accelerating voltage of 120 kV and the SEM images were collected by a Philips XL-30 FESEM. Also, magnetic measurements were carried out with a vibrating sampling magnetometer (VSM, Model 7400- LakeShore).

Preparation of Fe_2O_3 nanoparticles

$Fe(acac)_3$ was synthesized relevant to the general synthetic method in the literature [27]. For the synthesis of α-Fe_2O_3, the certain amount of the complex from the previous step was loaded into a crucible and then moved into the furnace. Nanoparticles of α-Fe_2O_3 were synthesized at 700 ºC after 8 h (S1). The yield was about 90%.

Preparation of $Fe_{2-x}Dy_xO_3$ nanoparticles

Three different $Dy_xFe_{2-x}O_3$ samples were synthesized in which x=0.01 (S_2), x=0.05 (S_3) or x=0.07 (S_4). Typically, for the synthesis of $Dy_{0.01}Fe_{1.99}O_3$, theoretically, 0.01 mmol of Dy^{3+} and 1.99 mmol of the Fe containing complex were loaded into a crucible and then moved into a preheated furnace. The reaction was performed at 700 °C for 8 h. Afterwards, the furnace was shut down and the obtained material was allowed to cool to the room temperature normally. The resulting reddish solid was collected for further studies. Analysis of the PXRD patterns revealed that by increasing the x to 0.07 mmol, Dy_2O_3 was loaded onto the crystal lattice of α-Fe_2O_3 and the doping process was failed.

Preparation of the electrode for electrochemical investigation

Nanopowder modified carbon paste electrodes were prepared by hand-mixing of 0.4 g of graphite powder and 0.1 g of pure and doped nanomaterial (prepared in different times) and paraffin at a ratio of 70/30 (w/w) and mixed well for 50 min until a uniformly wetted paste was obtained. Each

paste was then packed into a glass tube. Electrical contact was made by pushing a copper wire down the glass tube into the back of the mixture. When necessary, a new surface was obtained by pushing an excess of the paste out of the tube and polishing it on a weighing paper.

RESULTS AND DISCUSSION

Powder x-ray diffraction (PXRD)

Early structural characterization of the S_1, S_2, S_3 and S_4 was made by powder X-ray diffraction technique. Fig. 2 shows the PXRD pattern of pure α-Fe_2O_3 in the 2θ range 10-90°. The structural analyses performed by the *FullProf* program, is shown in Fig. 3(a-c). The structural analyses were performed employing profile matching with constant scale factors. Red lines are the observed intensities; the black ones are the calculated data; the blue ones are the difference: Yobs-Ycalc and Bragg reflections positions are indicated by blue bars. No peaks of any other phases or impurities were detected indicating high purity of the as-prepared α-Fe_2O_3 sample [27-30].

Fig. 4(a-d) shows the XRD patterns of S_1 to S_4. The XRD peaks at 2θ = 24.17°, 33.14°, 35.67°, 40.87°, 49.52°, 54.57°, 57.59°, 62.45° and 64.01° are assigned to the (012), (104), (110), (113), (024), (116), (122), (214) and (300) crystal planes, respectively. The XRD patterns of the samples (S_1-S_3) reveal that all peaks correspond to the characteristic peaks of the hexagonal structure of α-Fe_2O_3 with space group *R* according to the JCPDS data base number: 33-0664. With increasing the amount of Dy^{3+} from S_2 to S_3, no additional XRD lines pertaining to any secondary phase were observed. Since the ionic radius of Dy^{3+} and Fe^{3+} are 0.91 and 0.65 Å, respectively, this replacement is compensated by the reduction in the particles sizes [31]. By increasing the amount of Dy^{3+} to 0.07 (S_4), an additional peak at 2θ = 61.67º was

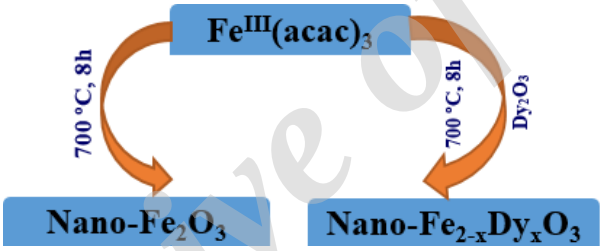

Fig. 1: Pure and Dy^{3+}-doped α-Fe_2O_3 nanoparticles synthesis process.

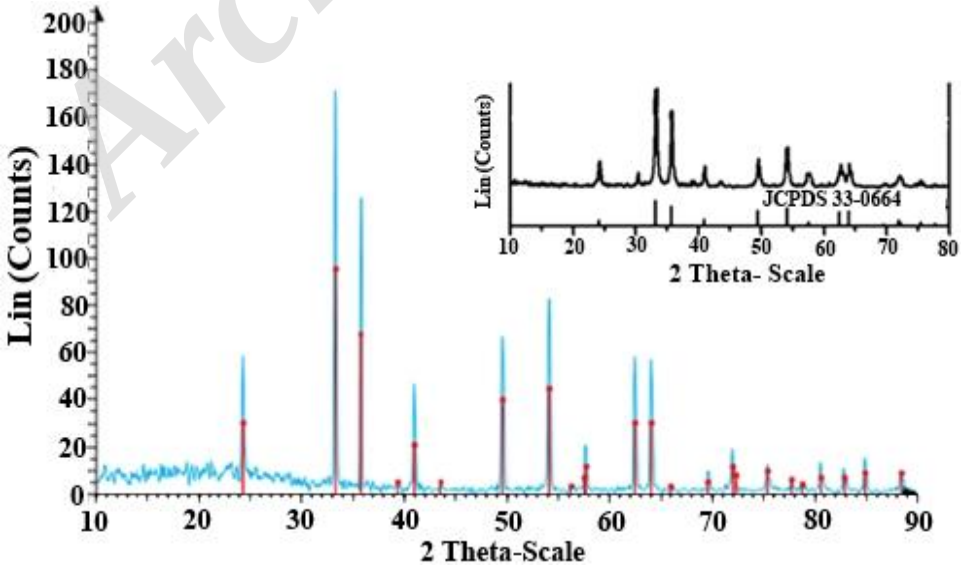

Fig. 2: XRD patterns of iron oxide (α-Fe_2O_3) obtained from combustion method at 700 °C for 8 h and JCPDS 33-0664 (inset).

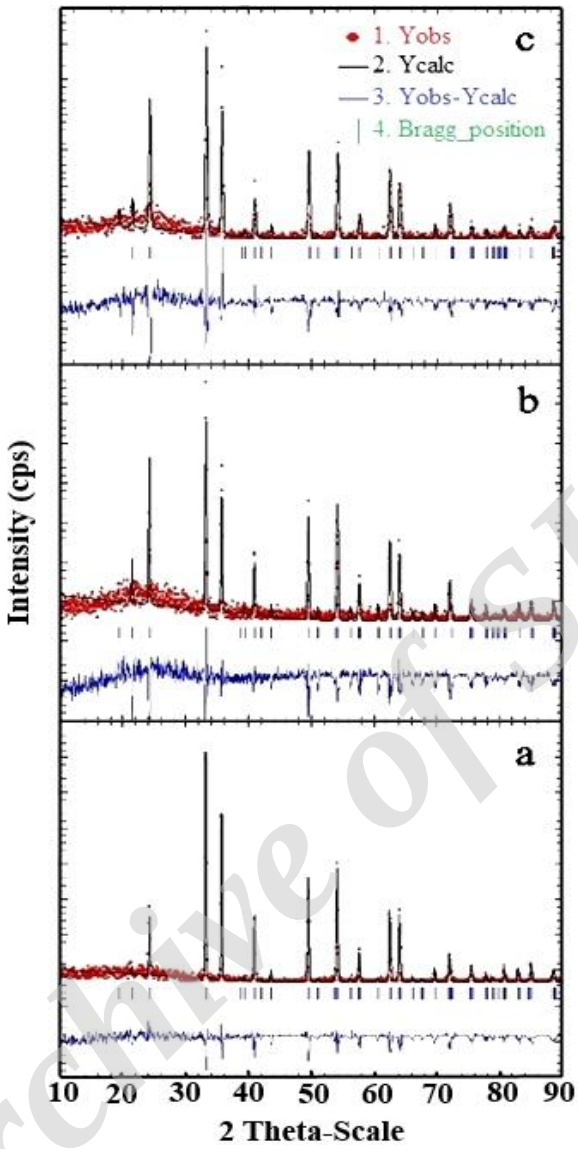

Fig. 3: Rietveld analysis of the synthesized nanomaterials.

observed. This additional peak is attributed to the excess of the Dy^{3+} ions which have resided on the surface or on the grain boundaries of the nanocrystals [32]. Thus, the maximum amount of Dy^{3+} in the α-Fe_2O_3 crystal structure is 0.05 mmol, theoretically. Besides, it is clear that a broad peak at 2θ = 20-40° is present with increasing the dopant amount in Fe_2O_3. Moreover, it shows that the amorphous phase formed in the material is increased with increasing the dopant amount. So, the crystalline phase amount of the material is decreased.

Table 1 shows the average crystallite sizes of S_1, S_2 and S_3 obtained from Scherer formula ($D = \frac{K\lambda}{B_{1/2}.\cos\theta}$) using the peak at hkl (104). D is the average crystalline size, λ is the X-ray diffraction wavelength (0.154 nm), K is the Scherrer constant (0.9), $B_{1/2}$ is the full-width at half-maximum (FWHM) of the diffraction peak and θ is the Bragg angle. The data mentioned in Table 1 show that the calculated crystallite size decreases with increasing the amount of dysprosium ion.

Table 2 shows the cell parameters and phase growth data for pure and doped Fe_2O_3 obtained by rietveld analysis. It was found that with doping Dy^{3+} into Fe_2O_3, the cell parameters were nearly

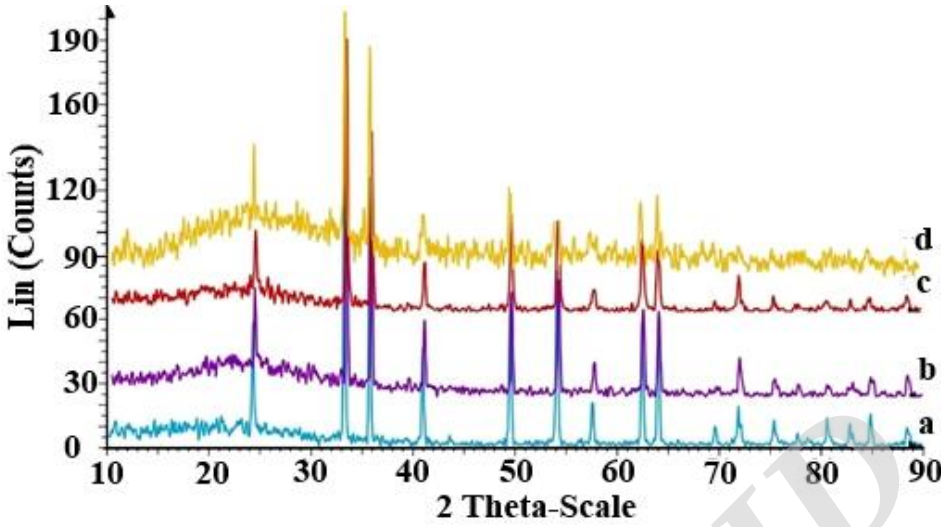

Fig. 4: XRD patterns of pure (a) and Dy^{3+} doped Fe_2O_3 in (b= 0.01, c = 0.05 and d = 0.07 mmol) obtained from combustion method at 700°C for 8 h.

Table 1: Crystallite size (D) and interplanar spacing (d) data for S_1, S_2 and S_3.

	S_1	S_2	S_3
2θ	33.1652	33.1646	33.1939
FWHM	0.1919	0.1476	0.1919
$B_{1/2}$	0.0033476	0.0025748	0.0033476
Cos θ	0.95840	0.95841	0.95834
D (nm)	43	56	43

constant. The quantitative phase analysis was also investigated with direct comparison method. In this method, we compared the experimental line intensity of Fe_2O_3 in the pure and doped materials PXRD patterns. For this purpose, we chose the peaks with the highest intensity at about 33°. The phase comparison values are summarized in Table 2. It shows that with doping Dy^{3+} into Fe_2O_3 (S_2) the intensity of the chosen peak was decreased. However, when the dopant amount was increased, the phase growth was improved, although the peak intensity of S_3 is still smaller than that for S_1.

Morphological investigation

The morphology of the pure and doped α-Fe_2O_3 was investigated by field emission scanning electron microscopy (FESEM) and transmission electron microscopy (TEM). Fig. 5(a-c) shows the FESEM images of S_1, S_2 and S_3, respectively. The morphologies of the α-Fe_2O_3 nanoparticles were almost spherical with some pores. However, it was found that by doping Dy^{3+} (S_2), the material morphology became spongy and there were no individual particles in the material. Besides, by increasing the dopant amount (S_3), the particles morphologies turned into almost particle and there was a big bulk morphology which was consistent with the PXRD data explained in the characterization section.

Fig. 6(a, b) show the TEM images of S_1 and S_3, respectively. Besides, for obtaining the exact average size of particles Fig. 7 shows the average particle size distribution profiles of S_1 and S_3 respectively. Fig. 7(a, b) show that the average particle sizes for S_1 and S_3 were about 125 and 60 nm, respectively. So, we can conclude that doping has caused a decreasing in the particles sizes. It is in agreement with the cell parameters data and interplanar spacing (d) values obtained from XRD patterns.

Table 2: Cell parameter data calculated from rietveld analysis.

Sample	*a* (Å)	*b* (Å)	Phase value (Intensity)	R_{Bragg}	R_F	χ^2
S_1	5.03109	13.74719	188.39	2.12	2.04	1.88
S_2	5.03085	13.72957	121.07	3.33	2.70	2.79
S_3	5.03105	13.73206	150.05	1.75	1.69	1.95

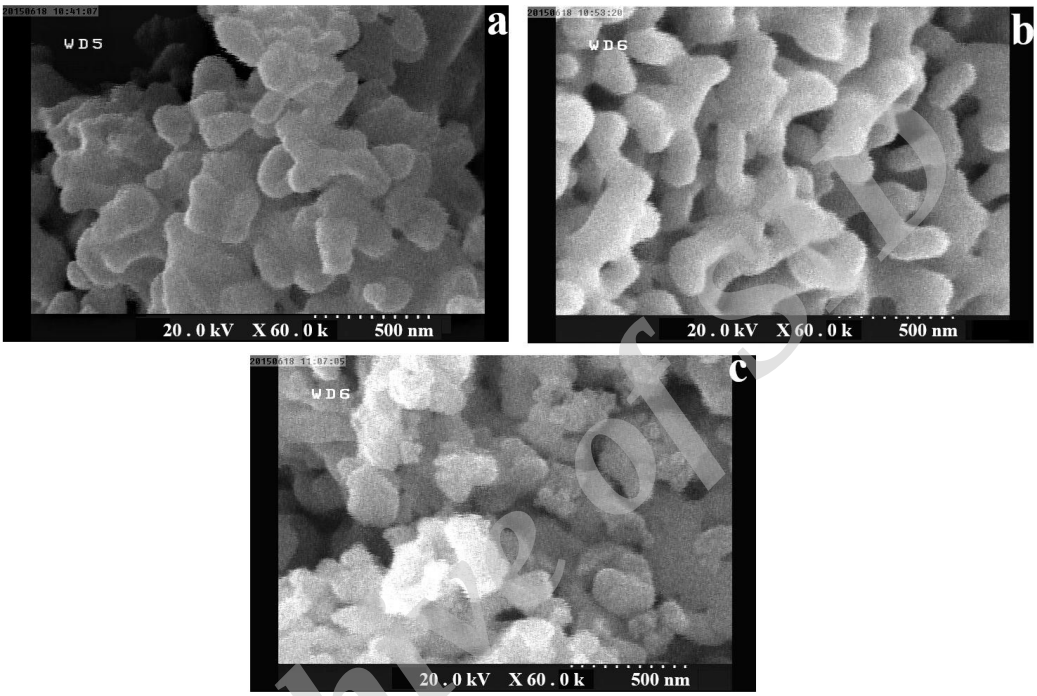

Fig. 5: FESEM images of a) S_1, b) S_2 and c) S_3.

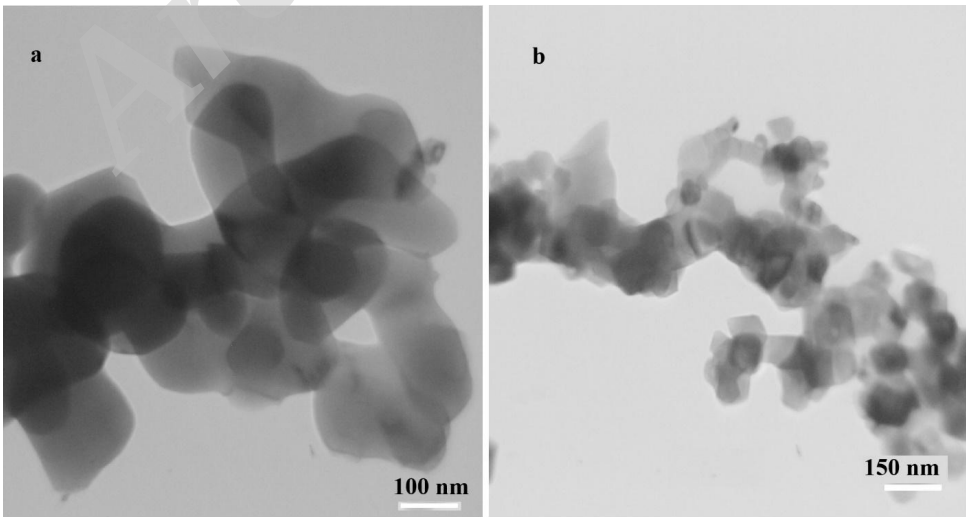

Fig. 6:TEM images of a) S_1 and b) S_3.

Previous reports show that the physical properties and morphology of nanomaterials strongly depend on the synthesis method. For example, it was found that the morphology of Fe_2O_3 was nanotube when using thermal decomposition and electrospinning methods [11, 16]; while the nano particle morphology was achieved when using emulsion precipitation method. Besides, particle morphology was obtained for the material by hydrothermal method at 160 ˚C. However, in the method, chitosan was used as a mediate for the preparation of the target. Hydrothermal and solvothermal methods at 200 ˚C for 24h also created particle morphology of the target [33, 34]. According to the data, the reaction temperature and time are the main factor on the size and morphology of the material. The present work represents efficient reaction time and temperature factors in the synthesis of α-Fe_2O_3 in particle and sponge morphology.

Elemental map and elemental analysis diagram for S_3 is shown in Fig. 8 (a, b), respectively. It can be seen from Fig. 8a that Dy, Fe and O elements are uniformly distributed in S_3. Also, Fig. 8b shows the EDS elemental analysis for S_3. The elemental analysis result shows that although the doping process was performed with x = 0.05 mmol of Dy^{3+}, the exact amount of the ion into the crystal system was x = 0.015 mmol. So, the experimental formula of S_3 is $Fe_{1.985}Dy_{0.015}O_3$.

FTIR spectra

The FT-IR spectra of $Fe(acac)_3$ complex and the synthesized α-Fe_2O_3 powder is shown in Fig. 9. The absorption peaks at 470 and 540 cm^{-1} can be attributed to the Fe-O stretching vibration modes in α-Fe_2O_3. These absorption peaks in the FTIR spectrum of α-Fe_2O_3 nanoparticles have shifted about 25 cm^{-1} to lower frequencies compared to $Fe(acac)_3$. The absorption peaks at 3427 and 1633 cm^{-1} can be assigned to the stretching vibration and bending vibration of OH groups of H_2O in α-Fe_2O_3. The absence of the stretching vibrations of C-H, C-O and other organic functional groups is also indicative of the successful preparation of α-Fe_2O_3 nanoparticles [31].

Electrochemical impedance spectroscopy

The electrical conductivity effects of the synthesized nanoparticles were investigated using electrochemical impedance spectroscopy (EIS). Electron transfer resistance, R_{ct} is an important factor for this goal. The semicircle portion at higher frequencies corresponded to the electron transfer limited process for a conductive surface or electroactive compound. Fig. 10 shows the impedance plots for (a) bare carbon paste electrode, (b) carbon paste electrode with S_3, and (c) carbon paste electrode with Fe_2O_3 nanoparticle in 1.0 mM $[Fe(CN)_6]^{3-/4-}$ (1 : 1) solution in 0.1 M KCl. It is evident from the EIS data that, at a surface of carbon paste electrode modified with Fe_2O_3, the resistance to electron transfer was at its minimum value that is relative to high conductivity effect of Fe_2O_3 at the surface of the electrode. Also, the R_{ct} for carbon paste electrode modified with S_3 is higher than that of Fe_2O_3. This shows that doping of Dy^{3+} has reduced electrical conductivity

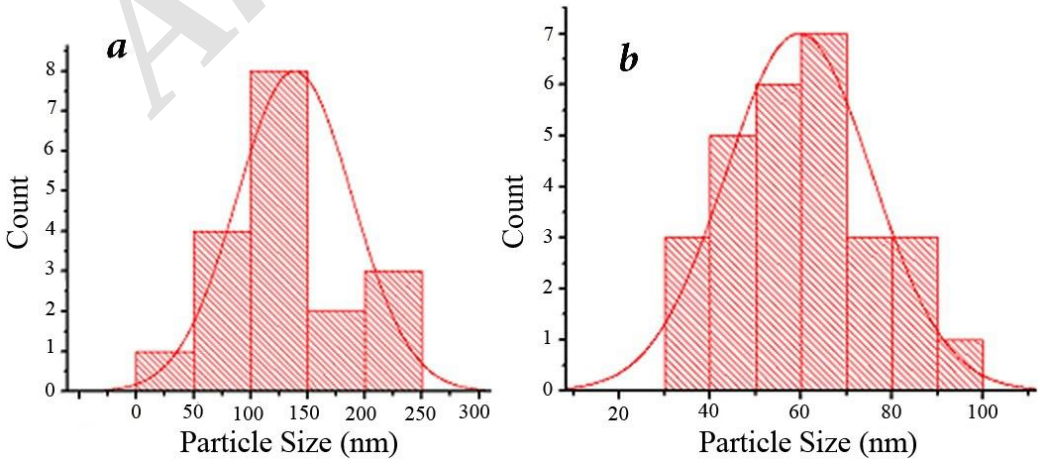

Fig. 7: Average particle size distribution profiles of a) S_1 and b) S_3.

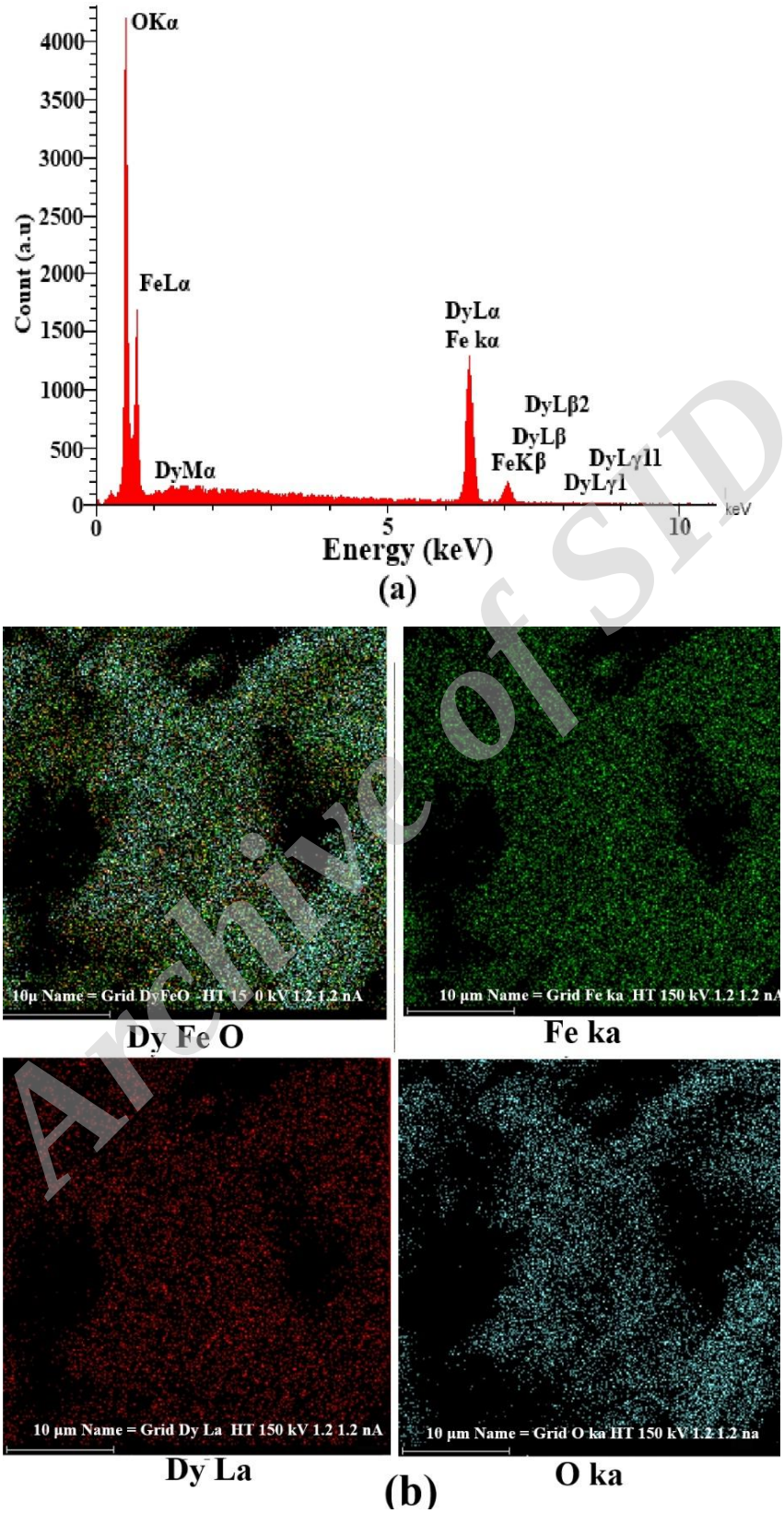

Fig. 8: a) Elemental analysis map and b) elemental analysis for S_3.

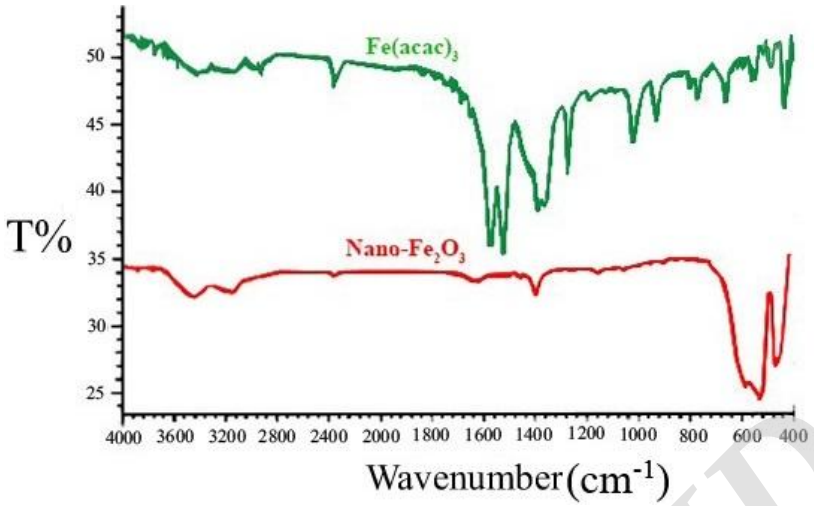

Fig. 9: FTIR spectrum of α-Fe_2O_3 nanoparticles and $Fe(acac)_3$ complex.

nanoparticles.

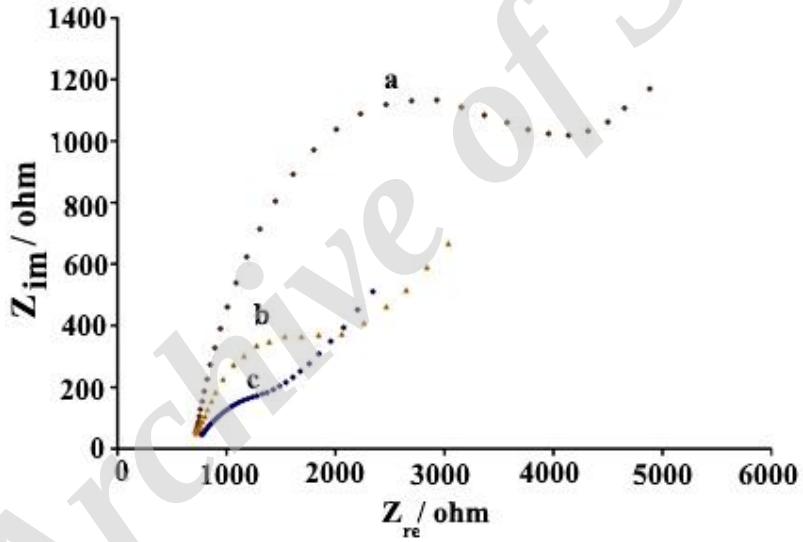

Fig. 10: Nyquist diagrams of 1 mM $K_4[Fe(CN)_6]$ in the presence of 0.1 M KCl. (a) bare carbon paste electrode, (b) carbon paste electrode with $Fe_{1.95}Dy_{0.05}O_3$, and (c) carbon paste electrode with Fe_2O_3 nanoparticle.

of Fe_2O_3 and the value of charge transfer resistance was increased. The present data confirm good electrical conductivity of Fe_2O_3 and $Fe_{1.95}Dy_{0.05}O_3$

Magnetization

Fig. 11 shows the magnetization curves of S_1 and S_3. To understand the magnetic properties, samples were measured by vibrating sample magnetometer (VSM) according to the applied field (M vs. H) at room temperature.

No saturation was observed for Fe_2O_3 sample up to field strengths of 20 KG. The existence of hysteresis loop in Fe_2O_3 with the remanent magnetization (Mr) of 0.244 emu/g and coercivity (Hc) of 4312 G shows ferromagnetic behavior. With the addition of Dy^{3+} in $Fe_{2-x}Dy_xO_3$ system, the coercivity was decreased and the remanent magnetization was increased, abruptly. These results are summarized in Table 3. The low hysteresis loop and reduced coercivity are similar to the behavior of superparamagnetic materials, which correspond to the behavior of particle size

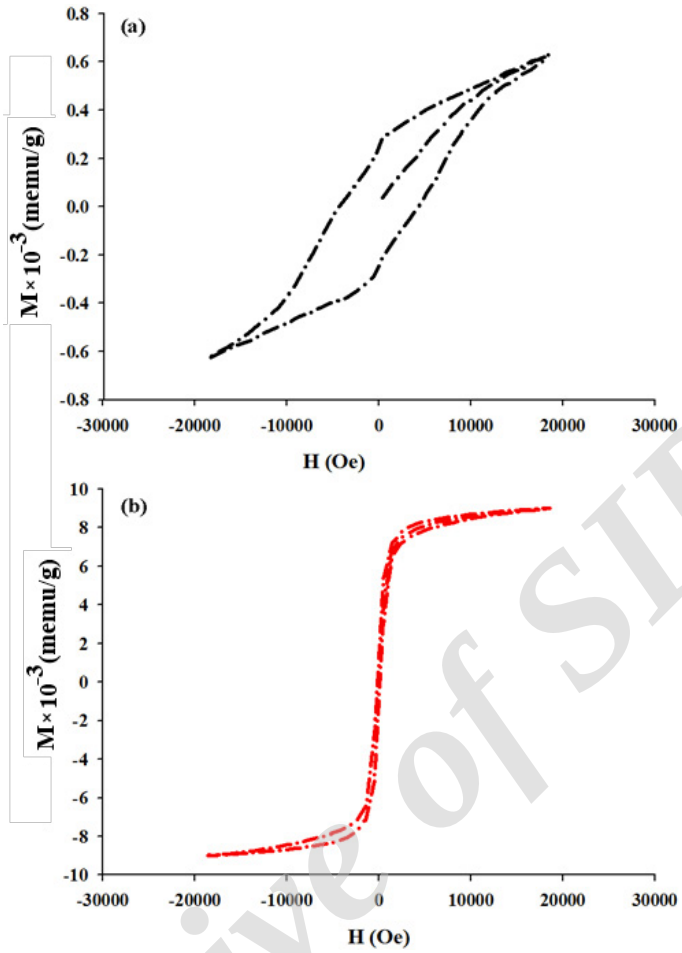

Fig. 11: Magnetization measurements at room temperature of $Fe_{2-x}Dy_xO_3$ nanostructure in x = 0.0 (a), and 0.05 Dy^{3+} (b).

Table 3: Remanent magnetization (Mr) and coercive force (Hc) for S_1 and S_3.

Sample	$-H_C$(G)	H_C(G)	$-M_r$(emu/g)	M_r(emu/g)	Average particle size (nm)
S_1	4333	4312	0.246	0.244	37.85
S_3	125	109.57	0.931	1.035	37.17

reduction. According to Table 3, we see that the samples with larger sizes have a large value of Hc compared to the samples with smaller size particles [35]. Rabanal *et al*. [36] have reported an H_C value of 576 Oe for a particle size of 80 nm. Huang *et al*. [37] have reported the coercivity value as 165G for 10 nm particle. A comparison of these data indicates a direct relationship between coercivity and particle size. Besides, increase in the amount of the remnant magnetization can be attributed to an increase in Dy^{3+} that is a magnet combination.

CONFLICT OF INTEREST

The authors declare that there is no conflict of interests regarding the publication of this manuscript.

CONCLUSIONS

In this work, combustion synthesis method was employed for preparing pure α-Fe_2O_3 and Dy^{3+}-

doped α-Fe_2O_3 nanoparticles. Nearly spherical nanoparticles of α-Fe_2O_3 was prepared by combustion of $Fe(acac)_3$ complex at 700 °C for 8 h. The structure and morphology of the synthesized nanoparticles were studied. The absence of any organic groups or other phases indicated the high purity of the as-prepared α-Fe_2O_3 nanoparticles. TEM images showed that the materials had spherical morphology in α-Fe_2O_3, while, in the $Fe_{2-x}Dy_xO_3$ two types of morphologies were detected, i.e. particle and spongy morphologies. Also, it was found that with the addition Dy^{3+} into the Fe_2O_3 crystal structure, the average particle size decreased. Magnetization measurements showed that with the addition of Dy^{3+}, the coercivity was reduced which confirmed the superparamagnetic behavior. The influence of dysprosium addition on electrochemical process was also studied using electrochemical impedance spectroscopy method. This study showed that by increasing dysprosium, the charge transfer resistant in electrochemical process decreased.

REFERENCES

[1] Xinghong W., Li Z., Yonghong N., Jianming H., Xiaofeng C., (2009), Fast preparation, characterization, and property study of α-Fe_2O_3 nanoparticles via a simple solution combusting method. *J. Phys. Chem*. 113: 7003-7008.

[2] Kesavan V., Sivanand P. S., Chandrasekaran S., Koltypin Yu., Gedanken A., (1999), Catalytic aerobic oxidation of cycloalkanes with nanostructured amorphous metals and alloys. *Angew. Chem. Int. Ed.* 38: 3521-3523.

[3] Huo L. H., Li W., Lu L. H., Cui H. N., Xi S. Q., Wang J., Zhao B., Shen Y. C., Lu Z. H., (2000), Preparation, structure, and properties of three-dimensional ordered α-Fe_2O_3 nanoparticulate film. *Chem. Mater*. 12: 790-794.

[4] Suresh K., Patil K. C., (1993), A combustion process for the instant synthesis of γ-iron oxide. *J. Mater. Sci. Lett*. 12: 572-574.

[5] Kroell M., Pridoehl M., Zimmermann G., Pop L., Odenbach S., Hartwig A., Magn J., (2005), Magnetic and rheological characterization of novel ferrofluids. *J. Magn. Mater*. 289: 21-24.

[6] Kang Y. S., Risbud S., Rabolt J. F., Stroeve P., (1996), Synthesis and characterization of nanometer-size Fe_3O_4 and γ-Fe_2O_3 particles. *Chem. Mater*. 8: 2209-2211.

[7] Zhang S., Chen X. J., Gu C. R., Zhang Y., Xu J. D., Bian Z. P., Yang D., Gu N., (2009), The effect of Iron Oxide magnetic nanoparticles on smooth muscle cells. *Nanoscale Res. Lett.* 4: 70-77.

[8] Srivastava R., Yadav B. C., (2012), Nanaostructured ZnO, ZnO-TiO_2 and ZnO-Nb_2O_5 as solid-state humidity sensor. *Adv. Mat. Let.* 3: 197-203.

[9] Chen L., Pang X., Yu G., Zhang J., (2010), In-situ coating of MWNTs with sol-gel TiO_2 nanoparticles. *Adv. Mat. Lett.* 1: 75-78.

[10] Askarinezhad A., Morsali A., (2008), Syntheses and characterization of $CdCO_3$ and CdO nanoparticles by using a sonochemical method. *Mater. Lett.* 62: 478-482.

[11] Sun Z. Y., Yuan H. Q., Liu Z. M., Han B. X., Zhang X. R., (2005), A highly efficient chemical sensor material for H_2S : α-Fe_2O_3 nanotubes fabricated using carbon nanotube templates. *Adv. Mat.* 17: 2993-2997.

[12] Jing Z. H., Wang Y., Wu S. H., (2006), Preparation and gas sensing properties of pure and doped γ-Fe2O3 by an anhydrous solvent method. *Sens. Actuators*. 113: 177-181.

[13] Lee E. T., Jang G. E., Kim C. K., Yoon D. H., (2001), Fabrication and gas sensing properties of Fe_2O_3 thin film prepared by plasma enhanced chemical vapor deposition (PECVD). *Sens. Actuators Chem.* 77: 221-227.

[14] Lim I. S., Jang F. E., Kim C. K., Yoon D. H., (2001), Fabrication and gas sensing characteristics of pure and Pt-doped γ-Fe_2O_3 thin film. *Sens. Actuators.* 77: 215-220.

[15] Dai Z. R., Pan Z. W., Wang Z. L., (2003), Novel nanostructures of functional oxides synthesized by thermal evaporation. *Adv. Mat.* 13: 9-23.

[16] Zheng W., Li Z. Y., Zhang H. N., Wang W., Wang Y., Wang C., (2009), Electrospinning route for α-Fe_2O_3 ceramic nanofibers and their Gas sensing properties. *Mater. Res. Bull.* 44: 1432-1436.

[17] Segadaes A. M., (2006), Oxide powder synthesis by the combustion route. *Eur. Ceram. News Lett.* 9: 1-5.

[18] Mukasyan A. S., Rogachev A. S., (2008), Discrete reaction waves: Gasless combustion of solid powder mixtures. *Prog. Energy Comb. Sci.* 34: 377-416.

[19] Kleiman-Shwarsctein A., Huda M. N., Walsh A., Yan Y., Stucky G. D., Hu Y.-S., Al-Jassim M. M., McFarland E. W., (2010), Electrodeposited aluminum-doped α-Fe_2O_3 photoelectrodes: Experiment and theory. *Chem. Mater*. 22: 510-517.

[20] Kleiman-Shwarsctein A., Hu Y.-S., Forman A. J., Stucky G. D., McFarland E.W., (2008), Electrodeposition of α-Fe_2O_3 doped with Mo or Cr as photoanodes for photocatalytic water splitting. *J. Phys. Chem.* 112: 15900-15907.

[21] Glasscock J. A., Barnes P. R. F., Plumb I. C., Savvides N., (2007), Enhancement of photoelectrochemical hydrogen production from hematite thin films by the introduction of Ti and Si. *J. Phys. Chem*. 111: 16477-16488.

[22] Cesar I., Kay A., Gonzales Martinez J. A., Graetzel M., (2006), Translucent thin film Fe_2O_3 photoanodes for efficient water splitting by sunlight: Nanostructure-Directing effect of Si-Doping. *J. Am. Chem. Soc.* 128: 4582-4583.

[23] Ingler W. B., Baltrus J. P., Khan S. U. M., (2004), Photoresponse of p-type zinc-doped iron (III) oxide thin films. *J. Am. Chem. Soc.* 126: 10238-10239.

[24] Goyal G., Dogra A., Rayaprol S., Kaushik S. D., Siruguri V., Kishan H., (2012), Structural and magnetization studies on nanoparticles of Nd doped α-Fe_2O_3. *Mat. Chem. Phys*. 134: 133-138.

[25] Bahaa Abu-Zied M., Asiri A. M., (2014), Synthesis of Dy_2O_3 nanoparticles via hydroxide precipitation: Effect of calcination temperature. *J. Rare Earths.* 32: 259-264.

[26] Kanga J-G., Seog Gwagb J., Sohn Y., (2015), Synthesis and characterization of $Dy(OH)_3$ and Dy_2O_3 nanorods and nanosheets. *Ceram. Int*. 41: 399-4006.

[27] Pinkas J., Reichlova V., Zboril R., Moravec Z., Bezdicka P., Matejkova J., (2008), Sonochemical synthesis of amorphous nanoscopic iron (III) oxide from $Fe(acac)_3$. *J. Ultrason. Sonochem*. 15: 257-264.

[28] Almeida T., Fay M., Zhu Y. Q., Brown P. D., (2009), Process map for the hydrothermal synthesis of α-Fe_2O_3 nanorods. *J. Phys. Chem*. 113: 18689-18698.

[29] Zhang G. Y., Xu Y.Y., Gao D. Z., Sun Y. Q., (2011), α-Fe_2O_3 nanoplates: PEG-600 assisted hydrothermal synthesis and formation mechanism. *J. Alloys. Compd.* 509: 885-890.

[30] Zhang G. Y., Feng Y., Xu Y. Y., Gao D. Z., Sun Y. Q., (2012),

Controlled synthesis of mesoporous α-Fe_2O_3 nanorods and visible light photocatalytic property. *Mate. Res. Bull*. 47: 625-630.

[31] Darezereshki E., (2011), One-step synthesis of hematite (α-Fe_2O_3) nano-particles by direct thermal-decomposition of maghemita. *Mater. Lett.* 65: 642-645.

[32] Gu F., Wang Sh. F., Lu M. K., Zhou G. J., Xu D., Yuan D. R., (2004), Structure evaluation and highly enhanced luminescence of Dy^{3+}-doped ZnO nanocrystals by Li^+ doping via combustion method. *Langmuir*. 20: 3528-3531.

[33] Sahoo S. K., Agarwal K., Singh A. K., Polke B. G., Raha K. C., (2010), Characterization of γ- and a-Fe_2O_3 nano powders synthesized by emulsion precipitation-calcination route and rheological behaviour of a-Fe_2O_3. *Int. J. Eng. Sci. Tech.* 2: 118-126.

[34] ChangLiang H., HongYe Z., ZhenYu S., ZhiMin L., (2010), Chitosan-mediated synthesis of mesoporous α-Fe_2O_3 nanoparticles and their applications in catalyzing selective oxidation of cyclohexane. *Sci. China. Chem*. 53: 1502-1508.

[35] Yogi A., Varshney D., (2013), Magnetic and structural properties of pure and Cr-doped haematite: α-$Fe_{2-x}Cr_xO_3$ ($0 \le x \le 1$). *J. Adv. Ceram.* 2: 360-369.

[36] Rabanal M. E., Rez A. Va., Levenfeld B., Torralba J. M., (2003), Magnetic properties of Mg-ferrite after milling process. *J. Mater. Process. Technol.* 143: 470-474.

[37] Huang Y., Tang Y., Wang J., Chen Q., (2006), Synthesis of $MgFe_2O_4$ nanocrystallites under mild conditions. *Mater. Chem. Phys.* 97: 394-397.